

# Using Machine Learning for Scientific Discovery in Electronic Quantum Matter Visualization Experiments

Yi Zhang<sup>1,\*</sup>, A. Mesaros<sup>1,2,\*</sup>, K. Fujita<sup>3</sup>, S.D. Edkins<sup>1,4</sup>, M.H. Hamidian<sup>1,5</sup>, K. Ch'ng<sup>6</sup>, H. Eisaki<sup>7</sup>,  
S. Uchida<sup>7,8</sup>, J.C. Séamus Davis<sup>1,3,9</sup>, E. Khatami<sup>6</sup> and Eun-Ah Kim<sup>1</sup>

<sup>1</sup> LASSP, Department of Physics, Cornell University, Ithaca, NY 14853, USA.

<sup>2</sup> Laboratoire de Physique des Solides, CNRS, Université Paris-Sud, 91405 Orsay Cedex, France.

<sup>3</sup> CMPMS Department, Brookhaven National Laboratory, Upton, NY 11973, USA.

<sup>4</sup> Department of Applied Physics, Stanford University, Stanford, CA 94305, USA.

<sup>5</sup> Department of Physics, Harvard University, Cambridge, MA 02138, USA.

<sup>6</sup> Department of Physics and Astronomy, San Jose State University, CA 95192, USA.

<sup>7</sup> Institute of Advanced Industrial Science and Technology, Tsukuba, Ibaraki 305-8568, Japan.

<sup>8</sup> Department of Physics, University of Tokyo, Bunkyo-ku, Tokyo 113-0033, Japan.

<sup>9</sup> Tyndall National Institute, University College Cork, Cork T12R5C, Ireland.

\* These authors contributed equally to this work.

**Essentials of the scientific discovery process have remained largely unchanged for millennia<sup>1,2</sup>: systematic human observation of natural phenomena is used to form hypotheses that, when validated through experimentation, are generalized into established scientific theory. Today, however, we face major scientific challenges because automated scientific instrumentation and large-scale data acquisition are generating data sets of such volume and complexity as to defy human analysis. To achieve scientific discovery using these enormous empirical data sets will require new approaches<sup>3,4</sup>. A good example is modern visualization studies of electronic quantum matter (EQM) which yield dense arrays of electronic structure images that are often astonishingly complex at the atomic-scale<sup>5</sup>. Given the recent advances in machine learning (ML) studies of synthetic EQM data,<sup>6-17</sup> the outstanding challenge now is to engage ML with real EQM data. Here we report development and training of an array of artificial neural networks (ANN) designed to recognize different types of hypothesized order hidden in EQM image-arrays. The ANNs are used to analyze a large, experimentally-derived EQM image archive,**

**spanning a wide range of electron densities and energies, in carrier-doped cuprate Mott insulators. Remarkably, this ML system repeatedly and reliably discovers, throughout all these noisy and complex data, the features of a very specific ordered state of EQM. It discerns a lattice-commensurate, precisely four-unit-cell periodic, unidirectional, translational-symmetry-breaking state, consistent with those long predicted within strong-coupling theories of electronic liquid crystals<sup>18,19</sup>. This marks a breakthrough in the capability of ML to achieve physics discovery and suggests broad new avenues for the scientific method.**

**1** Automation of scientific apparatus and high capacity data-acquisition have revolutionized the empirical approach to many sciences<sup>3,4</sup> including for example astronomy, elementary particles, genomics, climatology, and quantum materials research. In many cases, the resulting “big” data sets have already become far too large for any team of human beings to examine in detail, are often created without objective conceptual procedures for how to extract the fundamental knowledge therein, and yet they contain unsurpassed empirical information on many scientifically, societally and economically important subjects. Novel scientific approaches are urgently required to deal with the issues of volume, complexity and objectivity in analysis of these enormous experimental data sets, so that they can be fully exploited to achieve scientific discovery for the benefit of society. Globally, this has motivated urgent research initiatives within and across disciplines, whose strategic objectives are to develop machine learning techniques for use directly in the scientific discovery process<sup>20</sup>. However, although holding out tremendous promise<sup>3,4</sup>, condensed matter physics discoveries by ML using experimental data archives have so far been lacking.

**2** Crystalline solids contain many different types of EQM and familiar among them are simple metals, semiconductors, ferromagnets, superconductors and density waves. These

have been well understood for decades<sup>21</sup> using theoretic approaches that describe each electron as a weakly interacting wave-like quantum state. Today's research frontier is concentrated, instead, on the exotic forms of EQM that emerge when electrons interact so strongly that they can no longer be considered as individual wave-like quantum states. These electrons often self-organize into complex and unanticipated new states of EQM including, for example, high temperature superconductors<sup>22,23</sup>, electronic liquid crystals<sup>18</sup>, fractionalized electronic fluids<sup>24</sup> and quantum spin liquids<sup>25</sup>. In these forms of EQM, astronomical numbers of strongly interacting electrons exhibit unprecedented "social" behaviors which are often difficult to predict and challenging to understand. Vast experimental data sets have begun to appear in this field, for example from real space ( $\mathbf{r}$ -space) visualization of EQM using spectroscopic imaging scanning tunneling microscopy (SISTM), from momentum space ( $\mathbf{k}$ -space) visualization of EQM using angle resolved photoemission (ARPES), or from modern X-ray and neutron scattering facilities. The resulting challenge is to develop ML strategies capable of scientific discovery using these enormous and complex experimental data structures from condensed matter physics.

**3** For example, the electronic structure of the  $\text{CuO}_2$  plane in the cuprate compounds supporting very high temperature superconductivity<sup>22</sup> (Fig. 1A) is one of the deepest problems in EQM studies today. With one electron per Cu site, strong Coulomb interactions between electrons produce charge localization in an antiferromagnetic Mott insulator (MI) state. Removing  $p$  electrons (adding  $p$  'holes') per  $\text{CuO}_2$  plaquette generates the 'pseudogap' phase<sup>26,27</sup>, a state with strongly depleted density-of-electronic states  $N(E)$  as  $E \rightarrow 0$  relative to the enhanced  $N(E)$  at a characteristic 'pseudogap' energy scale  $E = \Delta_1$  (Fig. 1A). Eventually, at higher  $p$ , the  $d$ -symmetry high temperature superconductivity appears and enhancement of its maximum critical temperature  $T_c$  is the long-term strategic goal for the whole field. The pseudogap phase, which appears to constrain the highest  $T_c$ , has defied microscopic identification for two decades. But in recent years it has been widely reported,

using both SISTM visualization<sup>5,22</sup> and X-ray scattering<sup>22,28</sup> that spontaneous spatial modulations of observables, i.e., the density wave states, occur throughout the pseudogap regime  $0.07 \lesssim p \lesssim 0.20$  (Fig. 1A and Methods section 1). A density wave (DW) state with wavevector  $\mathbf{Q}$  is described by a spatially modulating function  $A(\mathbf{r}) = D(\mathbf{r})\text{Cos}(\phi(\mathbf{r}) + \phi_0(\mathbf{r}))$ , where  $A(\mathbf{r})$  represents the density amplitude,  $\phi(\mathbf{r}) = \mathbf{Q} \cdot \mathbf{r}$  is the DW spatial phase at location  $\mathbf{r}$ ,  $\phi_0(\mathbf{r})$  represents effects of disorder and topological defects. The term  $D(\mathbf{r})$  is the DW form factor symmetry which, for a tetragonal crystal, has  $s$ -symmetry if it remains unchanged under 90-degree rotations and  $d$ -symmetry if changes sign thereby. For the cuprate DW state,  $D(\mathbf{r})$  exhibits prevalent  $d$ -symmetry<sup>29-32</sup>.

**4** One theoretical approach to understanding the existence of such a DW is based on the conventional picture of wave-like electronic quantum states. Mobile, weakly correlated, electrons in a crystal have momenta  $\mathbf{p}(E) = \hbar\mathbf{k}(E)$  where  $\mathbf{k}(E) = 2\pi/\lambda(E)$  and  $\lambda(E)$  is the electron's quantum wavelength. The electronic structure can be represented in  $\mathbf{k}$ -space, an abstract space spanned by all possible electron  $\mathbf{k}(E)$ . The Fermi surface is defined as the  $\mathbf{k}$ -space contour  $\mathbf{k}(E = 0)$  that separates the occupied from the unoccupied electronic states as  $T \rightarrow 0$ . DW states can then appear at a wavevector  $\mathbf{Q} = (\mathbf{k}_i(E = 0) - \mathbf{k}_f(E = 0))$  if the electron states  $\mathbf{k}_i(E)$  and  $\mathbf{k}_f(E)$  are "nested", meaning they both have very high  $N(E)$  and are connected by the same wavevector  $\mathbf{Q}$  (red arrow Fig. 1B). Under these circumstances,  $\mathbf{Q}$  should usually be incommensurate and should vary rapidly with varying  $p$  (Fig. 1B and Methods section 1). An alternative class of theory holds that strongly interacting particle-like electrons<sup>33</sup> may be fully localized in the MI phase, or self-organized into electronic liquid crystal states<sup>18,19,33</sup> in  $\mathbf{r}$ -space. Many such EQM states have been discussed in theory<sup>33</sup>, but a typical example exhibits spatially periodic charge density modulations that are crystal-lattice-commensurate, having wavelength  $\lambda = 4a_0$  or wavevector  $\mathbf{Q} = \frac{2\pi}{a_0}(0.25,0)$  oriented along the Cu-O-Cu axis (Fig. 1C and Methods section 1). Such lattice-commensurate, unidirectional charge modulations in particle-like theories (Fig. 1C) are

expected to be robust against changes with electron-density  $p$  and electron-energy, while those associated with the geometry of Fermi surface in wave-like theories (Fig. 1B) are expected to evolve continuously with  $p$ .

**5** Although it is crucial to discriminate between these particle-like or wave-like theoretic perspectives, this has not been achieved because the cuprate DW state is profoundly disordered at the nanometer scale<sup>5,22,26-29</sup>. This can be seen directly in a typical image of cuprate electronic structure at  $E=\Delta_1$  as shown in Fig. 1D. A fundamental long-term challenge has therefore been to determine if the spatial arrangements of electronic structure in hole-doped  $\text{CuO}_2$  (e.g. Fig. 1E) are lattice-commensurate, unidirectional, with specific wavevectors, or if they evolve continuously with electron-density and electron-energy. The extreme disorder observed in all extensive atomic-scale EQM images<sup>5</sup>, or concomitantly the broad and fluctuating line-widths detected in reciprocal space<sup>18,22,26,28</sup>, have prevented a clear answer to this key question. Indeed, theory shows that conventional Fourier analysis of such noisy and disordered EQM images is fundamentally limited<sup>34,35</sup> in the valid inference than can be drawn on the exact symmetries of this EQM state.

**6** High-data-volume imaging studies of EQM (e.g. Fig. 1E) use SISTM, a technique that allows probabilistic visualization of the density-of-electronic-states  $N(\mathbf{r}, E)$  with sub-atomic resolution and crystal-lattice register. The resulting image-array for a given sample is built up from measurements of STM-tip-sample differential electron tunneling conductance  $dI/dV(\mathbf{r}, V) \equiv g(\mathbf{r}, V)$  at a square array of locations  $\mathbf{r}$  and at a range of tip-sample voltage differences  $V$ . In theory,  $g(\mathbf{r}, V) \propto N(\mathbf{r}, E) / \int_0^{eV_s} N(\mathbf{r}, E) dE$  for  $E=eV$  and  $V_s$  is the arbitrary junction-formation bias<sup>5</sup>. Thus, visualization of the spatially-resolved and energy-resolved  $N(\mathbf{r}, E)$  – one of the most powerful modern tools for EQM studies – becomes possible. Note that even if  $\int_0^{eV_s} N(\mathbf{r}, E) dE$  is heterogeneous and thus  $g(\mathbf{r}, V)$  is not simply related to  $N(\mathbf{r}, E)$ , the ratio  $Z(\mathbf{r}, V) = g(\mathbf{r}, +V)/g(\mathbf{r}, -V)$  may be used

as a valid measure of EQM spatial symmetry because the denominators of  $g(\mathbf{r}, +V)$  &  $g(\mathbf{r}, -V)$  cancel each other. Fourier analysis of  $Z(\mathbf{r}, V)$  to yield  $Z(\mathbf{q}, V)$  is then the obvious approach to determining the EQM modulation wavevectors, however, because of the nanoscale spatial disorder (Fig. 1D), the relevant maxima in Fourier reciprocal space ( $\mathbf{q}$ -space) are so broad and fluctuate so widely as to be inconclusive. Overall then, the process of going from an array of such  $Z(\mathbf{r}, E = eV)$  images (e.g. Fig. 1E) to identifying and understanding the fundamental broken-symmetry state of EQM hidden therein, is highly non-trivial. Moreover, there is typically no established manual scheme of regression to achieve that objective.

7 Development of a ML strategy capable of recognizing hidden EQM ordered states and identifying their broken-symmetries in such atomic-scale electron structure image-arrays could be a breakthrough in pinpointing the ordering scenario of the EQM. Although impressive ML-based progress has already been made in the recognition of quantum many-body wavefunctions in synthetically generated EQM data<sup>6-17</sup>, the profound challenge we now face is to develop ML techniques capable of achieving scientific discovery with non-synthetic experimental EQM data sets. Required are general tools for manipulation and analysis of EQM image-arrays, allied with the ability to include human-generated hypotheses into the machine learning process, plus the fundamental capability of ML to identify the key physical phenomena contained in the data. The long-term objectives are to develop a ML strategy capable of recognizing specific EQM states in real (automated, heterogeneous, noisy, incomplete) experimental image-arrays, and to establish reliable functionality of such ML strategy for EQM studies, so that they can become the norm in physics labs of the future. Here we introduce a specific ML system using ANN's to achieve hypothesis testing with EQM image-arrays, based upon supervised ML within an ANN-human coalition. Its goal is to automatically search experimental EQM image-arrays from SISTM experiments (e.g. Fig. 1E), to recognize spatial modulations in a variety of distinct

categories, to identify their fundamental periodicity and lattice register throughout an image, and eventually to distinguish if the modulations are unidirectional or bidirectional. Our ML strategy has three stages.

**8** The first stage is to generate the sets of ANN training images, each labeled by an hypothesis: the different DW states to be discerned. We test four hypotheses associated with four distinct types of periodic modulations, all with a d-symmetry form factor, and with fundamental wavevectors  $\mathbf{Q}=0.23,0.25,0.27,0.29(2\pi/a_0,0)$  respectively. Four training sets for each category  $C=1,2,3,4$  are then generated by introducing specific forms of heterogeneity designed to mimic the noise, intrinsic disorder and topological defects of experimental data (Fig. 2A, see Methods section 2). Throughout these simulated training-image-sets, the heterogeneity disrupts the long-range ordered patterns in  $\mathbf{r}$ -space as shown for a typical example of a training image in Fig. 2B. It also scrambles the peaks in the d-symmetry Fourier transforms<sup>5</sup> of the training images, rendering them broad and chaotic (Fig. 2C). We also allow for the ANN's to declare "none of the above" through the zeroth category  $C=0$ . The training set for category  $C=0$  is generated by pixel-averages of randomly selected images belonging to above four categories as well as corresponding images with  $|\mathbf{Q}|=2\pi/a_0$  and samples of white noise.

**9** The second stage is to decide on an ANN architecture that trains well with the above training-image-sets. During training, the parameters of the ANN are adjusted iteratively to minimize the cost function (a measure of the distance between the ANN outcome and the training set label)<sup>36</sup>. In supervised machine learning, one trains each ANN by minimizing the cross-entropy cost function that quantifies the difference between the ANN output and the associated label for all images within the training-image-set. To achieve this goal, each ANN evaluates an output for a given training set input, and then its parameters (the ANN weights and biases) are adjusted through stochastic gradient descent and back

propagation<sup>37</sup> to lower the cost function. The training is complete when the cross-entropy<sup>38</sup> saturates, and the finalized ANN generally has an accuracy >99% on validation images (Fig. 2D) (see Methods section 3). Our choice of ANN design is a fully connected feed forward network with a single hidden layer (Fig. 3C) (see Methods section 3). Statistical reliability of this ML system against different network architectures and different initial conditions is then achieved by training 81 distinct ANNs in parallel with the same training image-set.

**10** The final stage is to hypothesis test the experimental EQM image-array using the above ensemble of trained networks. We first employ the trained ANN's to identify effects of the change in the average electron-density within the EQM data. This consists of an array of measured  $Z(\mathbf{r}, E)$  electronic-structure images from samples of the hole-doped cuprate  $\text{Bi}_2\text{Sr}_2\text{CaCu}_2\text{O}_8$  that span the range of electron density  $0.06 < p < 0.20$ . Specifically, the measured  $Z(\mathbf{r}, E)$  images have FOV  $16\text{nm} \times 16\text{nm}$  at electron-densities  $p \approx 0.06, 0.07, 0.09, 0.20$  ( $T_c(\text{K}) = 20, 45, 50, 82$ ). The ANNs analyze images  $Z(\mathbf{r}, E = \Delta_1)$  as a function of  $p$ , focusing on the pseudogap energy  $E = \Delta_1(p)$  at each electron-density because, at this energy, the symmetry-breaking exhibits maximum amplitude in the cuprate EQM. Figures 4A-D show the actual  $Z(\mathbf{r}, E = \Delta_1)$  images presented to the trained ANN system while Figs. 4E-H show their  $d$ -symmetry Fourier transforms. As the experimental field of view and resolution is typically different for each image-array, we developed a procedure for a careful preparation of the data to standardize the ANN input (see Methods section 4). Obviously disorder and complexity of EQM abound in  $Z(\mathbf{r}, E = \Delta_1)$  throughout this whole electron-density range (black double headed arrow in Fig. 1A) and are equally apparent in the broad fluctuating peaks around  $(Q_x \pm \delta Q_x, \delta Q_y)2\pi/a_0$  and  $(\delta Q_x, Q_y \pm \delta Q_y)2\pi/a_0$  in  $Z(\mathbf{q}, E = \Delta_1)$  (see Figs.3A,B). One realizes the serious challenge to determine a fundamental modulation wavevector (if extant) in such images because there are no sharp features whatsoever. Indeed, it would appear highly unlikely to human perception that a well-defined DW with a specific modulation-wavevector could even be



hidden in these images. Remarkably, however, the ANN's succeed in discriminating and identifying the key wavevectors in these images (see Methods section 5). In Figures 4I-L we show the response of the ANNs as the probability  $P(C)$  that the presented EQM image is identified in the category  $C$ . Strikingly, the ANNs conclude that, on the average, the training-image with the highest probability of being recognized throughout the  $Z(\mathbf{r}, E)$  image-array for almost all different electron-densities at which DW state is established in this material is  $C=2$ . The ML system thus recognizes broken translational symmetry, and distinguishes that this occurs commensurately with the specific wavevector  $\mathbf{Q} = (2\pi/4a_0, 0)$  for electron densities up to the highest presented (Fig. 4A-E). Accordingly, the identical, commensurate, broken translational-symmetry DW state was hidden throughout these EQM image-arrays, that span a swathe of the  $\text{CuO}_2$  electronic phase diagram (Fig. 1A).

**11** A second key physics issue is the energy dependence within an  $Z(\mathbf{r}, E)$  image-array. Quasiparticle scattering interference<sup>5</sup> (QPI) occurs when an impurity atom scatters wave-like states  $\mathbf{k}_i(E)$  into  $\mathbf{k}_f(E)$ , resulting in quantum interference at wavevectors  $\mathbf{Q}_{if}(E) = \mathbf{k}_i(E) - \mathbf{k}_f(E)$ , and generating modulations of the density-of-states  $\delta N(\mathbf{r}, E)$  or its Fourier transform  $\delta N(\mathbf{Q}_{if}, E)$ . QPI is a distinct physical phenomenon from a DW state because in the former modulation wavevectors evolve rapidly with electron-energy  $\mathbf{Q}_{if}(E)$  where in the latter they are non-dispersive or independent of electron-energy. Therefore, the ANNs explore a  $\text{Bi}_2\text{Sr}_2\text{CaCu}_2\text{O}_8$   $Z(\mathbf{r}, E)$  array of 16nmX16nm EQM images, in a range of electron-energy  $E=36,66,96,126$  (meV) for  $p=0.08$  ( $T_c(\text{K})=45$ ). Figures 5A-D show this  $Z(\mathbf{r}, E)$  image set (all acquired simultaneously) that is presented to the same ANN system. EQM complexity in the identical field of view now evolves rapidly with electron-energy because they are dominated by QPI. Similarly, Figures 5E-H are the  $d$ -symmetry Fourier transforms  $Z(\mathbf{q}, E)$  from Figures 5A-D, showing broad fluctuating peaks around  $(Q_x \pm \delta Q_x, \delta Q_y)2\pi/a_0$  and  $(\delta Q_x, Q_y \pm \delta Q_y)2\pi/a_0$ . But now  $\delta Q_x, \delta Q_y$  evolve rapidly with electron-energy, another quantum mechanical effect expected in QPI. From these  $Z(\mathbf{r}, E)$  (A-D) and  $Z(\mathbf{q}, E)$  (E-H),

well-defined fundamental modulation-wavevector hidden in these images appears indiscernible. However, figures 5I-L demonstrate the responses of the ANN suite as the probability  $P(C)$ . The hypothesis category with the highest probability of being recognized is again in  $C=2$  for all energies, meaning that the ANN's identify the predominant modulations at all energies to have wavevector  $|\mathbf{Q}|=2\pi/4a_0$  (Fig. 5A-D). Again, the ANN's recognize a hidden, commensurate, translational broken-symmetry state at  $\mathbf{Q} = (2\pi/4a_0, 0)$ , for all energies presented despite intense masking by QPI phenomena.

**12** To summarize: we have developed and demonstrated a new general protocol for ML-based identification of the translational symmetry-breaking ordered states in electronic structure image-arrays from EQM visualization experiments. In this human-ANN coalition, traditional human insight into orders and symmetries forms the basis of the training-image generation (Fig. 2). The ANN's are then trained to learn the defining traits of each category (ordered state) and to process the image array recognizing those traits in real EQM image arrays. Despite extreme complexity of the EQM state, instrument distortion and noise, the intense crystal and electronic disorder of the EQM image array studied (Figs. 1, 2), the trained ANN's repeatedly and reliably discover predominant features of a very specific ordered state with lattice-commensurate,  $4a_0$  periodic, unidirectional, translational-symmetry breaking (Figs. 4 and 5). In fact, the power of our ML strategy is demonstrated in the remarkable universality and simplicity of the fundamental physics it reveals, underlying the highly complex EQM image-arrays presented. As an advance in CM physics, the predominance of modulations at all electron-densities and independent of electron-energy of lattice-commensurate and unidirectional DW with wavevector  $\mathbf{Q} = (2\pi/4a_0, 0)$  implies that a particle-like theory is fundamentally required to describe the broken-symmetry states of doped  $\text{CuO}_2$ . Concurrently, a milestone for scientific discovery has been achieved with the demonstration that ANN's can process and identify

specific broken symmetries of highly complex image-arrays from non-synthetic experimental EQM data, through an ANN-human coalition. Overall, these combined advances open the immediate and exciting prospect of additional ML-driven scientific discovery in EQM studies.

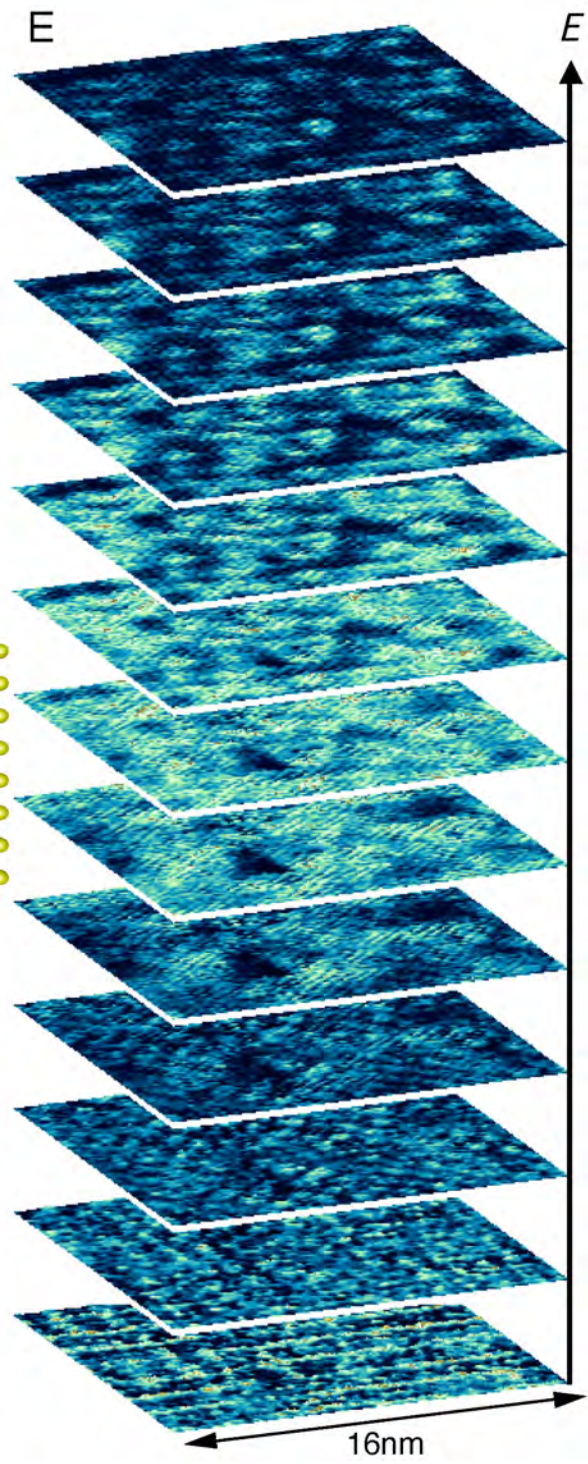
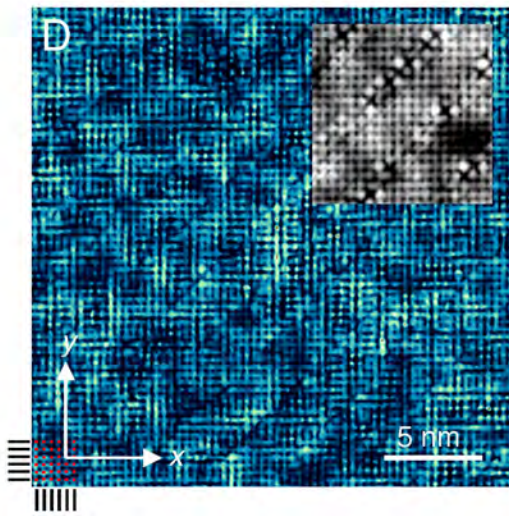
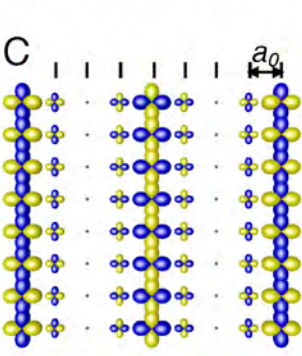
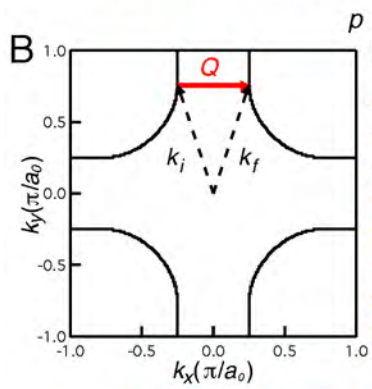
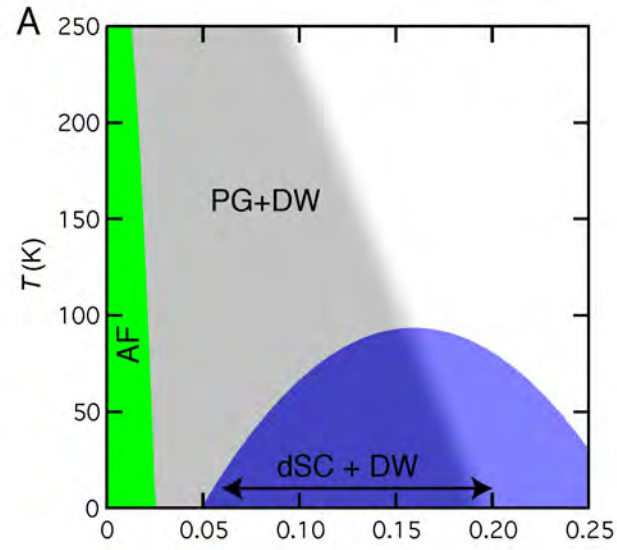


**Figure 1. Electronic quantum matter imaging in hole-doped CuO<sub>2</sub>.** **A**, Schematic phase diagram of hole-doped CuO<sub>2</sub>. At  $p=0$  a single electron is localized at each Cu site and all are arranged in long-range antiferromagnetic (AF) order. As holes are introduced (electrons removed) the AF order quantum melts quickly. The high temperature superconductivity (SC) emerges at slightly higher  $p$ , reaching its maximum critical temperature  $T_c$  near  $p \sim 0.16$ . However, in the range  $p < 0.2$  an enigmatic phase of EQM, dubbed the pseudogap (PG) phase, is known to contain periodic charge density modulations of imprecise wavevector  $\mathbf{Q}$ . **B**, In the CuO<sub>2</sub> Brillouin zone, the Fermi surface is defined as the  $\mathbf{k}$ -space contour  $\mathbf{k}(E = 0)$  that separates the occupied from unoccupied electronic states, and its locus changes rapidly with changing carrier density  $\rho$ . Density wave (DW) states may then appear at a wavevector  $\mathbf{Q}(\mathbf{k}_i(E = 0) - \mathbf{k}_f(E = 0))$  if the electron states  $\mathbf{k}_i(E)$  and  $\mathbf{k}_f(E)$  are "nested" (red arrow). **C**, Strongly correlated electrons may be fully localized in the Mott insulator phase, or self-organized into electronic liquid crystal states<sup>18,33</sup> in  $\mathbf{r}$ -space. Schematically shown here is a simple example of a state with unidirectional charge density modulations in the CuO<sub>2</sub> plane, having wavelength  $\lambda = 4a_0$  or wavevector  $\mathbf{Q} = \frac{2\pi}{a_0}(0.25, 0)$  (Methods section 1). **D**, Typical 24.4nmX24.4nm SISTM image of electronic structure  $R(\mathbf{r}, E = 150\text{mV})$  from the CuO<sub>2</sub> plane of Bi<sub>2</sub>Sr<sub>2</sub>CaCu<sub>2</sub>O<sub>8</sub> with  $p=0.08$  ( $T_c=45\text{K}$ ). Complex spatial patterns, which to human visual perception look like highly disordered "tweed", dominate. The contrast with simple periodic arrangement of the simultaneously visualized atoms of the same crystal in the topograph (upper inset) is arresting. **E**, Typical image-array of simultaneously measured  $Z(\mathbf{r}, E)$  for  $p=0.08$ , each 16nmX16nm but at a different electron energy  $E$ , spanning the range  $6\text{meV} < E < 150\text{meV}$  in steps of 12 meV. Such arrays are the basic type of data-set for which efficient ML analysis and discovery techniques are urgently needed.

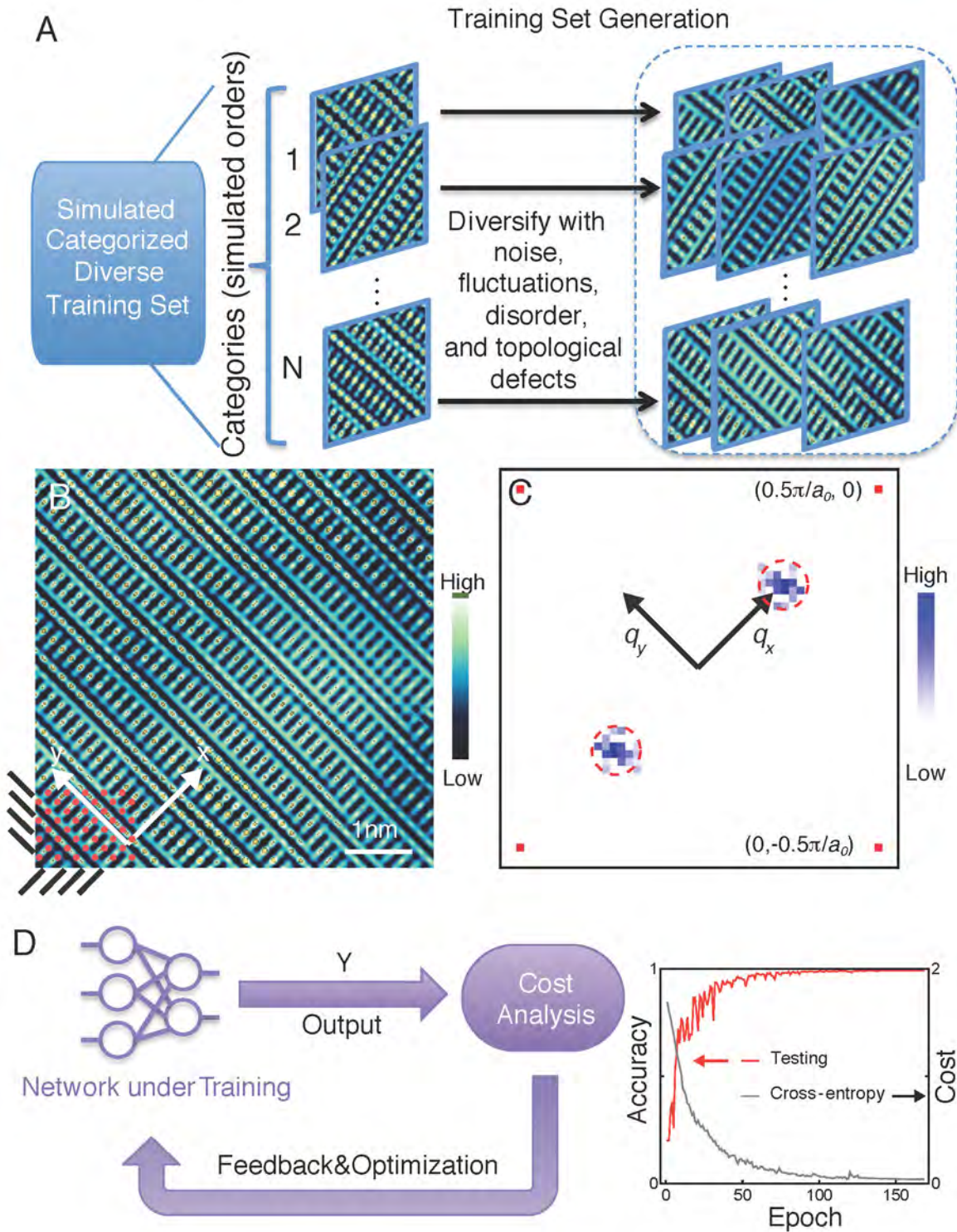


**Figure 2. Training ANN to identify broken-symmetry states in SISTM data. A,** The ANN array is trained to recognize a DW in electronic structure images (e.g.  $Z(\mathbf{r}, E)$ ) representing different EQM states. A synthesized training-image set for the ANNs is obtained by appropriately diversifying pristine images of 4 distinct electronic ordered states. Each translational symmetry-breaking ordered state is labeled by a category  $C = 1, 2, 3, 4$  associated with its wavevector:  $Q_C = 0.23, 0.25, 0.27, 0.29(\frac{2\pi}{a_0}, 0)$  respectively. The training-images in each category are diversified by appropriate addition of noise, short correlation-length fluctuations in amplitude and phase, and topological defects. **B,** Example of a training-image in category  $C=2$  which is a  $d$ -symmetry form factor (dFF) DW with  $Q = 0.25(\frac{2\pi}{a_0}, 0)$  within which smooth amplitude and phase fluctuations and randomized positions of topological defects (discommensurations) have been added to simulate typical phenomena encountered in experimental EQM visualization (e.g. 1D). The 516x516 pixel image contains 2x86x86 entire  $\text{CuO}_2$  unit-cells with Cu-Cu distance of 6 pixels diagonally. **C,** The  $d$ -symmetry Fourier transform of **B**. Absence of a well-defined modulation wavevector  $Q$  within the modulations in **B** has been successfully simulated in the training-image as seen by the region of  $q$ -space (red dashed circle) within which strong variation in the amplitudes at different wavevectors occur. Red marks are at  $q = \left[\frac{2\pi}{a_0}\right] (\pm 0.5, 0); (0, \pm 0.5)$ . **D,** Each ANN is trained by minimizing the cross-entropy cost function progressively through stochastic gradient descent and back propagation. The process of going through the entire set of shuffled training data, also known as an epoch, is repeated until the cross-entropy and accuracy saturate. The overall accuracy of the finalized ANNs on the synthesized data is generally over 99%.

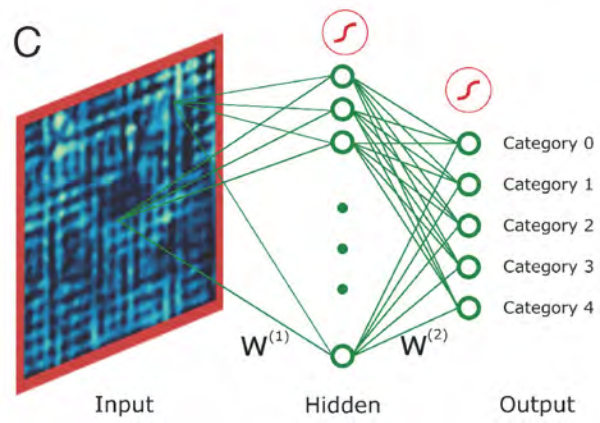
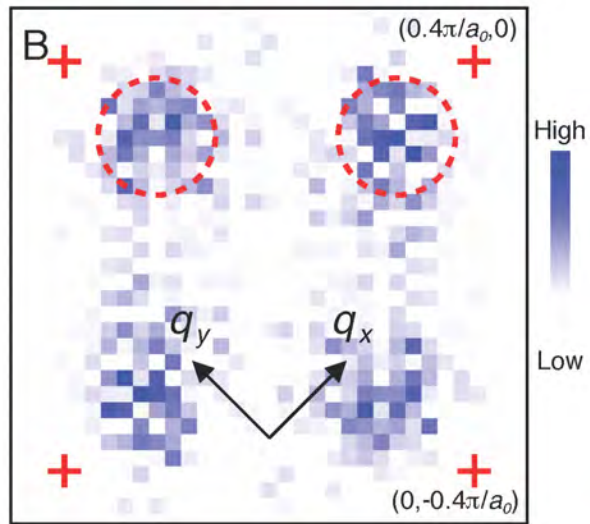
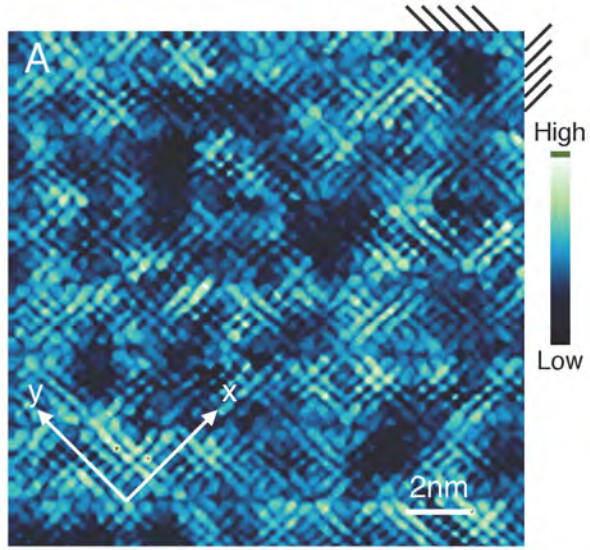




**Figure 3. ANN analysis of experimental EQM visualization data.** **A**, Typical measured 16nmX16nm  $Z(\mathbf{r}, E = 84\text{meV})$  image of  $\text{Bi}_2\text{Sr}_2\text{CaCu}_2\text{O}_8$  with  $\rho=0.08$  ( $T_c=45\text{K}$ ). The disorder and complexity of EQM are vivid. **B**, Typical measured  $Z(\mathbf{q}, E = 84\text{meV})$  image of  $\text{Bi}_2\text{Sr}_2\text{CaCu}_2\text{O}_8$  with  $\rho=0.08$  ( $T_c=45\text{K}$ ) being the d-symmetry Fourier transform of **A**. The disorder and complexity of EQM are equally vivid here in the broad and fluctuating peaks around  $(Q_x \pm \delta Q_x, \delta Q_y)2\pi/a_0$  and  $(\delta Q_x, Q_y \pm \delta Q_y)2\pi/a_0$  with  $|\delta Q_x| = |\delta Q_y| \approx 0.2$ . Red crosses are at the  $(0.4, 0); (0, 0.4)2\pi/a_0$  points. **C**, Schematic of ANN analysis procedure for experimental  $Z(\mathbf{r}, E)$  images: the successfully trained neural network with fixed parameters (weights  $W^{(1)}$  and  $W^{(2)}$  of the hidden layer and the output layer respectively and biases) is a classifier: It classifies each experimental image as belonging into one of the five categories. We take statistics of independent assessment on the given experimental image by 81 ANN's that are independently trained to arrive at the probabilities  $P(C)$  of the image belonging to category C.

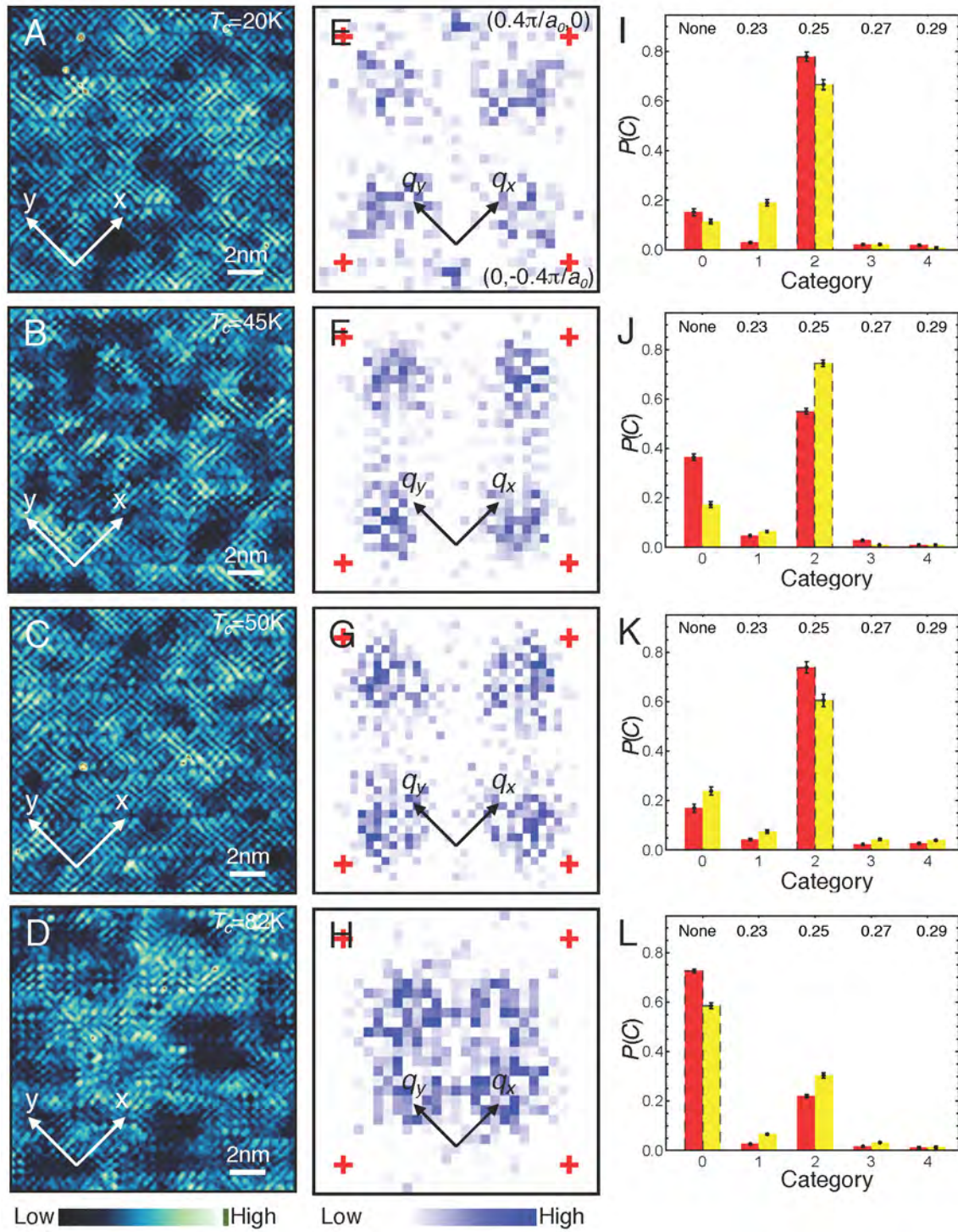


**Figure 4. ANN detection of broken-symmetry evolution with electron-density. A-D,** Measured 16nmX16nm  $Z(\mathbf{r}, E)$  images of  $\text{Bi}_2\text{Sr}_2\text{CaCu}_2\text{O}_8$  in a range of electron densities with  $p=0.06, 0.07, 0.09, 0.20$  ( $T_c(\text{K})=20, 45, 50, 82$ ). Each image is measured at  $E = \Delta_1(p)$  the pseudogap energy at that electron-density because it is where the symmetry breaking exhibits maximum amplitude. Obviously disorder and complexity of cuprate EQM abound throughout this whole electron-density range (black double headed arrow in Fig. 1A). **E-H,** The  $d$ -symmetry Fourier transforms  $Z(\mathbf{q}, E)$  from **A-D**. The disorder and complexity of EQM are equally vivid as broad fluctuating peaks around  $(Q_x \pm \delta Q_x, \delta Q_y)2\pi/a_0$  and  $(\delta Q_x, Q_y \pm \delta Q_y)2\pi/a_0$ . Red crosses are at the  $(0.4, 0); (0, 0.4)2\pi/a_0$  points. **I-L,** Output categorization by 81 ANNs of the preprocessed images from **A-D**. Top row numbers: the length of category's fundamental wavevector, in units of  $\frac{2\pi}{a_0}$ . Since the training-images for ANNs are unidirectional, i.e., their pristine orders have wavevectors  $\vec{Q}_c = Q_c \vec{e}_x$ , categorizations result for two modulation orientations X,Y (red and yellow bars) are obtained by inputting to ANNs the preprocessed  $Z(\mathbf{r}, E)$  image-array and its 90-degree rotated version, respectively.

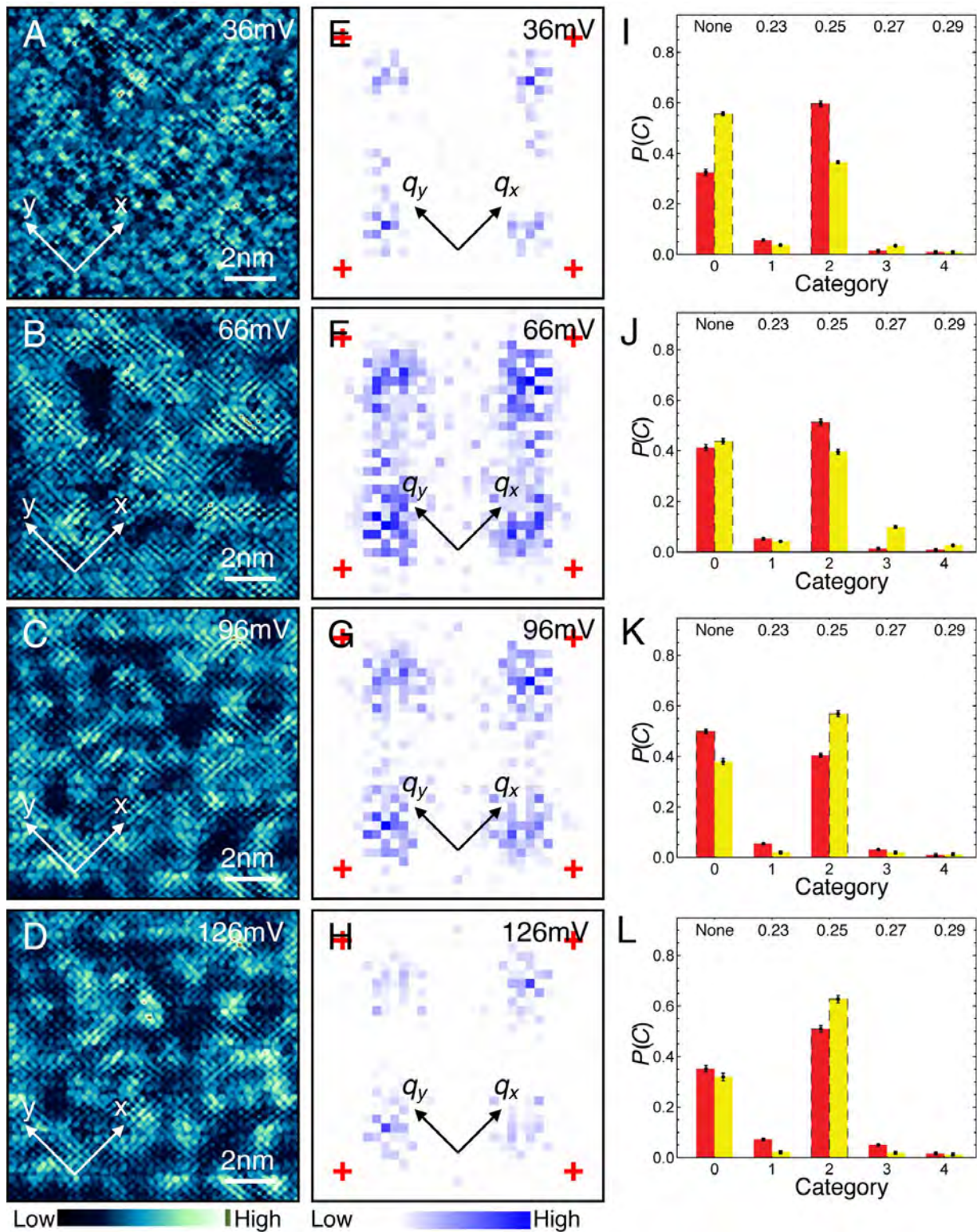


**Figure 5. ANN detection of broken-symmetry at different electron-energies. A-D,** Measured 16nmX16nm  $Z(\mathbf{r}, E)$  images of  $\text{Bi}_2\text{Sr}_2\text{CaCu}_2\text{O}_8$  in a range of electron-energy  $E=36,66,96,126$  (meV) for  $p=0.08$  ( $T_c(\text{K})=45\text{K}$ ). EQM complexity in the identical field of view, now evolves rapidly with electron-energy, a purely quantum mechanical effect. **E-H,** The  $d$ -symmetry Fourier transforms  $Z(\mathbf{q}, E)$  from **A-D**. The disorder and complexity of EQM are strong as seen in the broad fluctuating peaks around  $(Q_x \pm \delta Q_x, \delta Q_y)2\pi/a_0$  and  $(\delta Q_x, Q_y \pm \delta Q_y)2\pi/a_0$  but now  $\delta Q_x, \delta Q_y$  evolve rapidly with electron-energy (another quantum mechanical effect). Red crosses occur at  $(0.5,0); (0,0.5)2\pi/a_0$  points. **I-L,** Output categorization by 81 ANNs of the preprocessed images from **A-D**. Top row numbers: the length of category's fundamental wvector, in units of  $\frac{2\pi}{a_0}$ . Categorization results for two modulation orientations X,Y (red and yellow bars) are obtained by inputting to ANNs the preprocessed  $Z(\mathbf{r}, E)$  image-array and its 90-degree rotated version, respectively.

## **Acknowledgements**

We thank Paul Ginsparg, Jenny Hoffman, Steve Kivelson, Andy Millis, Roger Melko, Miles Stoudenmire, Kilian Weinberger, Jan Zaanen for helpful discussions and communications. E.-A.K., A.M., and Y.Z. acknowledge support from DOE DE-SC0010313; E.-A.K. and Y.Z. acknowledge support from DOE DE-SC0018946; S.U. and H.E. acknowledge support from a Grant-in-aid for Scientific Research from the Ministry of Science and Education (Japan) and the Global Centers of Excellence Program for Japan Society for the Promotion of Science. E.K. acknowledges support from the NSF Grant No. DMR-1609560. E.-A.K. and E.K. acknowledge support from the Kavli Institute for Theoretical Physics, supported in part by the NSF under Grant No. PHY-1748958, where initial discussions about the project took place. K.F. and J.C.S.D. acknowledge support from the U.S. Department of Energy, Office of Basic Energy Sciences, under contract number DEAC02-98CH10886. S.D.E, M.H.H and J.C.S.D. acknowledge support from the Moore Foundation's EPiQS Initiative through Grant GBMF4544. J.C.S.D. acknowledges the hospitality of Tyndall National Institute, University College Cork, IRL.

**Author Information** Reprints and permissions information is available at [www.nature.com/reprints](http://www.nature.com/reprints). The authors declare no competing financial interests. Readers are welcome to comment on the online version of the paper. Correspondence and requests for materials should be addressed to E.-A. K.; [eun-ah.kim@cornell.edu](mailto:eun-ah.kim@cornell.edu)

## References

---

- 1 *De Partibus Animalium*, Aristotle; Lennox, J. G. (Clarendon Press, Oxford U.P.)
- 2 *On Floating Bodies*, Archimedes; Heath, T. L. (Cambridge U.P., Cambridge, 1912).
- 3 Gil, Y., Greaves, M., Hendler, J., Hirsh, H. Amplifying Scientific Discovery with Machine Learning. *Science* **346**, 171 (2014).
- 4 AI is Changing How We Do Science, doi:10.1126/science.aan7049 (2017)
- 5 Fujita, K. *et al*, *Spectroscopic Imaging STM: Strongly Correlated Systems - Experimental Techniques* pp 73-109. Springer-Verlag Berlin Heidelberg (2015).
- 6 Carrasquilla, J. and Melko, R. G. Machine learning phases of matter. *Nature Physics* **13**, 431(2017).
- 7 Wang, L. Discovering phase transitions with unsupervised learning. *Phys. Rev. B* **94**, 195105 (2016).
- 8 Carleo, G. and Troyer, M. Solving the quantum many-body problem with artificial neural networks. *Science* **355**, 602 (2017).
- 9 Torlai, G. and Melko, R.G. Neural decoder for topological codes. *Phys. Rev. Lett.* **119**, 030501 (2017).
- 10 Van Nieuwenburg, E. P. L., Liu, Y.-H. and Huber, S. D. Learning phase transitions by confusion. *Nature Physics* **13**, 435-439 (2017).
- 11 Broecker, P., Carrasquilla, J., Melko, R. G. and Trebst, S. Machine learning quantum phases of matter beyond the fermion sign problem. *Scientific Reports* **7**, 8823 (2017).
- 12 Ch'ng, K., Carrasquilla, J., Melko, R. G. and Khatami, E. Machine Learning Phases of Strongly Correlated Fermions. *Phys. Rev. X* **7**, 031038 (2017).
- 13 Zhang, Y. and Kim, E.-A. Quantum loop topography for machine learning. *Phys. Rev. Lett.* **118**, 216401 (2017).
- 14 Deng, D.-L. , Li, X. and Das Sarma, S. Quantum entanglement in neural network states. *Phys. Rev. X* **7**,021021 (2017).

- 
- 15 Stoudenmire, E. M. and Schwab, D. J. Supervised learning with tensor networks. *Advances in Neural Information Processing Systems (NIPS)* **29**, 4799 (2016).
  - 16 Schindler, F., Regnault, N. and Neupert, T. Probing many-body localization with neural networks. *Phys. Rev. B* **95**, 245134 (2017).
  - 17 Torlai, G., Mazzola, G., Carrasquilla, J., Troyer, M., Melko, R. G. and Carleo, G. Neural-network quantum state tomography. *Nature Physics* **14**, 447 (2018).
  - 18 Kivelson, S. A., Fradkin, E. and Emery, V. J. Electronic liquid-crystal phases of a doped Mott insulator. *Nature* **393**, 550 (1998).
  - 19 Zaanen, J. Self-organized one dimensionality. *Science* **286**, 251 (1999).
  - 20 National Science Foundation's 10 Big Ideas (2016),  
[http://www.nsf.gov/news/special\\_reports/big\\_ideas/](http://www.nsf.gov/news/special_reports/big_ideas/)
  - 21 Ashcroft, N. W. and Mermin N. D. *Solid State Physics* (Brooks Cole, Boston, 1976).
  - 22 Keimer, B., Kivelson, S. A., Norman, M. R., Uchida, S. and Zaanen, J. From quantum matter to high-temperature superconductivity in copper oxides. *Nature* **518**, 179–186 (2015).
  - 23 Wang, F. and Lee, D.-H. The Electron-Pairing Mechanism of Iron-Based Superconductors. *Science* **332**, 200-204 (2011).
  - 24 Stormer, H. L., Tsui, D. C. and Gossard, A. C. The fractional quantum Hall effect. *Rev. Mod. Phys.* **71**, S298 (1999).
  - 25 Balents, L. Spin liquids in frustrated magnets. *Nature* **464**, 199–208 (2010).
  - 26 Orenstein, J. and Millis, A.J. Advances in the Physics of High-Temperature Superconductivity. *Science* **288**(5465):468–474 (2000).
  - 27 Norman, M. R., Pines, D. and Kallin, C. The pseudogap: friend or foe of high  $T_c$ ?. *Adv. Phys.* **54**, 715-733 (2005).
  - 28 Comin, R. and Damascelli, A. Resonant X-Ray Scattering Studies of Charge Order in Cuprates. *Ann. Rev. of Condensed Matter Physics* **7**:369-405 (2016).
  - 29 Fujita K. et al. Direct phase-sensitive identification of a d-form factor density wave in underdoped cuprates. *Proc. Nat'l. Acad. Sci.* **111**, E3026–E3032 (2014).



- 
- 30 Forgan, E. M. *et al.* The microscopic structure of charge density waves in underdoped  $\text{YBa}_2\text{Cu}_3\text{O}_{6.54}$  revealed by X-ray diffraction. *Nature Communications* **6**, 10064 (2015).
- 31 Comin R. *et al.* Symmetry of charge order in cuprates. *Nature Materials* **14**, 796–800 (2015).
- 32 Hamidian, M.H. *et al.* Atomic-scale electronic structure of the cuprate d-symmetry form factor density wave state. *Nature Physics* **12**, 150 (2016).
- 33 Fradkin, E., Kivelson, S. A. and Tranquada, J. M. Colloquium: Theory of intertwined orders in high temperature superconductors. *Rev. Mod. Phys.* **87**, 457 (2015).
- 34 Robertson, J. A. *et al.* Distinguishing patterns of charge order: Stripes or checkerboards. *Phys. Rev. B* **74**, 134507 (2006).
- 35 Del Maestro, A., Rosenow, B. and Sachdev, S. From stripe to checkerboard ordering of charge-density waves on the square lattice in the presence of quenched disorder. *Phys. Rev. B* **74**, 024520 (2006).
- 36 Nielsen, M. A. *Neural Networks and Deep Learning* (Determination Press, 2015); <http://neuralnetworksanddeeplearning.com>.
- 37 Rumelhart, D. E., Hinton, G. E. and Williams, R. J. Learning representations by back-propagating errors. *Nature* **323**, 533-536 (1986).
- 38 Cover, T. M., and Thomas, J. A. *Elements of Information Theory* (2nd Edition, Wiley, 1991).